Small-angle neutron scattering study on phase separation in a super duplex stainless steel at 300 C – Comparing hot-rolled and TIG welded material

Journal Item

Materials Characterization 190 (2022) 112044

Contents lists available at ScienceDirect

Materials Characterization

journal homepage: www.elsevier.com/locate/matchar

Small-angle neutron scattering study on phase separation in a super duplex stainless steel at 300 °C – Comparing hot-rolled and TIG welded material

Jianling Liu [a,*], Yadunandan Das [a,1], R. Prasath Babu [a], Sten Wessman [b], Jan Y. Jonsson [c], Joakim Odqvist [a], Stephen M. King [d], Peter Hedström [a]

[a] Department of Material Science and Engineering, KTH Royal Institute of Technology, SE-100 44 Stockholm, Sweden
[b] Swerim AB, P.O. Box 7047, SE-164 07 Kista, Sweden
[c] Outokumpu Stainless AB, Koppardalsvägen 71, 774 41 Avesta, Sweden
[d] ISIS Pulsed Neutron and Muon Source, STFC Rutherford Appleton Laboratory, Harwell Campus, Didcot OX11 0QX, United Kingdom

ARTICLE INFO

Keywords:
Duplex stainless steels
TIG welding
Small-angle neutron scattering (SANS)
Phase separation
Focused ion beam - digital image correlation (FIB-DIC)
Residual strain

ABSTRACT

The evolution of nanoscale phase separation in the ferrite phase of super duplex stainless steel 25Cr—7Ni (wt%) (SDSS 2507) and two SDSS TIG (tungsten inert gas) weldments have been quantitatively investigated by small-angle neutron scattering (SANS). The results show that the phase separation is more pronounced in the SDSS weldments in comparison to the base metal SDSS 2507, especially after aging for 35,000 h at 300 °C. These results correlate with the higher ferrite micro-hardness in the aged TIG weldments than in the SDSS 2507. The enhanced phase separation is partly due to the higher contents of Cr and Ni in the ferrite of TIG weldments compared to SDSS 2507 base metal, revealed by energy-dispersive X-ray spectroscopy (EDS). Additionally, the residual strain measurements through focused ion beam and digital image correlation (FIB-DIC), indicate larger residual strains in the ferrite of weldments than in the base metal SDSS 2507. This is also believed to contribute to the enhanced phase separation.

1. Introduction

Super duplex stainless steel 25Cr—7Ni (wt%) (UNS S32750), containing a balanced ferrite (bcc) to austenite (fcc) ratio, possesses good weldability and an attractive combination of strength and corrosion resistance [1,2]. The application of these steels and their weldments are, however, limited to a maximum service temperature of about 250 °C as they suffer from the notorious '475 °C embrittlement', leading to significant changes in mechanical properties such as hardness and toughness [3,4]. This problem may be severe during long-term exposure at service temperatures [5]. This embrittlement is due to ferrite phase decomposition, also referred to as phase separation (PS), where the initially homogeneous bcc phase decomposes into a highly coherent nanostructure of Fe-rich (α) and Cr-rich (α') phases [6]. Extensive investigations have been performed to study the effect of various parameters such as alloying [7], thermal cycles [8,9], grain boundaries [10] and dislocations [11], on the kinetics of PS. Most of the work has been performed on simple laboratory alloys such as binary and ternary Fe—Cr based alloys, but more works are also appearing on advanced multicomponent alloys such as duplex stainless steel (DSS).

Welding is quite important for the application of DSS [12–14], and super duplex stainless steel 25Cr—7Ni (SDSS 2507) generally demonstrate good weldability. However, welding may cause degradation of the mechanical properties if severe grain coarsening and/or the formation of excessive ferrite or intermetallic phases occur in the weld metal (WM) and/or heat affected zone (HAZ) of the DSS welds [15]. In order to achieve superior weldments, recommendations for DSS welding operation should be followed [13]. The common welding methods used for DSS involve tungsten inert gas (TIG), metal inert gas (MIG), or submerged arc welding (SAW) [13]. For thick plates of SDSS 2507, TIG welding is considered a good choice as it limits the heat input so that the fast cooling rate can avoid the formation of unwanted phases, e.g. intermetallic phases [13], and also limit ferrite grain coarsening. During TIG welding, filler materials with higher Ni content, and some nitrogen addition in the shielding gas, are used to promote austenite re-formation and increase the corrosion resistance. Considering these aspects, high welding speeds and narrow joint configurations can be achieved while obtaining the desired microstructure [13,15].

* Corresponding author.
E-mail address: jianling@kth.se (J. Liu).
[1] Presently at: The Open University, Walton Hall, Milton Keynes MK7 6AA, United Kingdom.

https://doi.org/10.1016/j.matchar.2022.112044
Received 19 January 2022; Received in revised form 2 June 2022; Accepted 5 June 2022
Available online 8 June 2022

Table 1
Chemical composition of welds, BM and filler material (wt%).

Material	Fe	C	Si	Mn	P	Cr	Ni	Mo	Cu	N
Weld-1	Bal.	0.012	0.38	0.74	0.018	26.3	7.9	4.3	0.15	0.24
Weld-2	Bal.	0.015	0.36	0.75	0.017	26.1	7.6	4.2	0.16	0.25
2507	Bal.	0.015	0.24	0.83	0.023	24.8	6.9	3.8	0.23	0.27
27.9.5.L	Bal.	0.016	0.40	0.76	<0.020	27.1	8.8	4.5	0.12	0.30

In spite of careful procedures during welding, DSS weldments are extra sensitive to the '475 °C embrittlement' during service [16]. An atom probe study by Zhou et al. [12] revealed that the PS in the TIG weld bead 25.10.4 L was much more pronounced than in the base DSS SAF 2507 after aging at 325 °C for 3000 h. Hosseini et al. [17] showed that in SDSS 2507 the WM showed faster kinetics of PS than the base metal (BM) at 475 °C. On the other hand, a recent study from Hosseini et al. [11] compared the kinetics of PS between base plates and welds of SDSS 2507 aged only for 5 min at 475 °C and they found conflicting results with Zhou et al. [12]: the hot-rolled SDSS plates had initially faster kinetics of PS than the SDSS welds. It should be noted that their welds had been solution annealed so that the expected residual strain levels should be different from a normal weld. It is also uncertain whether such studies under extreme accelerated conditions can be used to represent real-service conditions, e.g. there can be significant differences with respect to recovery and stress relaxation, microstructural coarsening and formation of other phases such as G-phase, comparing e.g. 475 °C and 300 °C.

A few studies [18,19] have dealt with the effect of TIG welding on the DSS microstructure. However, its influence on specifically the subsequent nanostructural evolution at low temperatures, i.e. through PS, has not been elucidated. A more quantitative comparison of BM and WM in SDSS 2507 is needed to investigate the effect of TIG welding on the kinetics of PS during long-term aging at relevant service temperatures. Das et al. [20] have recently outlined a method for efficient quantification of PS in DSS using small-angle neutron scattering (SANS) data. That method allows for quantitative bulk characterization with high sensitivity towards minor PS, not attainable by standard nanoscale characterization methods such as transmission electron microscopy (TEM) [21].

This study aims to apply the quantitative methodology proposed by Das et al. [20] to investigate the phase separation in SDSS 2507 base metal and two SDSS TIG-weldments. The underlying mechanisms affecting the change of PS kinetics in DSS weldments are sought, and hence, the SANS analysis has been supplemented by micro-hardness measurements, microstructural characterization and residual strain analysis.

2. Experimental methodology

2.1. Materials and heat treatment

The materials were supplied by Outokumpu Stainless AB. The BM SDSS 2507 was isothermally aged at 300 °C for up to 48,000 h, whereas the weldments, which are more susceptible to PS, were only aged for 35,000 h at 300 °C. The weldments, Weld-1 and Weld-2, both joined two 17.8 mm-thick SDSS 2507 plates using the TIG method. The filler material 27.9.5.L was used and an inter-pass temperature of ~100 °C as well as N_2 shielding gas was applied. The chemical composition of the two weldments, analysed by glow-discharge optical emission spectroscopy (GDOES) plus melt extraction for C and N, is shown in Table 1. The nominal composition of the BM and filler materials are included in Table 1 as well. Weld-1 was designed to have 15 welding passes while Weld-2 only had 11 passes. During the TIG welding, the total heat input for Weld-1 is 11.4 kJ/mm and for Weld-2 11.7 kJ/mm. Due to the different number of welding passes, the average heat input per pass for Weld-1 and Weld-2 is 0.76 and 1.07 kJ/mm, respectively.

2.2. Microscopy

Light optical microscopy (LOM) on the microstructures of BM, HAZ and WM of Weld-1 and Weld-2 were obtained using an Olympus PMG 3. A modified Beraha II solution consisting of 100 mL water, 50 mL HCl and 0.5 g $K_2S_2O_5$ was used for etching to reveal the austenite and ferrite in the samples. Electron backscatter diffraction (EBSD) and energy-dispersive X-ray spectroscopy (EDS) were performed using a JEOL JSM-7800F field-emission gun scanning electron microscope (FE-SEM), equipped with Bruker e-Flash^{HR} EBSD detector and Bruker XFlash 6–30 EDS detector. The software Bruker Quantax was used for data acquisition and post-processing of EBSD and EDS data. Prior to the EBSD/EDS measurements, specimens were exposed to polishing with 0.02 μm colloidal silica and then electro-polished in a 10 wt% $HClO_4$ – Ethanol solution at room temperature using a voltage of 20 V.

2.3. Hardness testing and modeling

2.3.1. Micro-hardness measurements

The micro-hardness of ferrite has a strong relation with the extent of PS during aging at low or intermediate temperatures [5]. In order to investigate the hardness evolution in the ferrite and austenite, Vickers micro-hardness measurements within the ferrite and austenite phases were performed using a Qness Q10 micro-hardness tester with a small load of 5 *g* on the transverse section of the fusion zone of the weld specimens. The diagonal of the indentation is 5 μm for each phase. Prior to micro-hardness measurements, the specimens were polished down to 0.25 μm diamond finish and lightly etched using a solution of 100 mL HCl, 10 mL HNO_3 and 100 mL H_2O to reveal the boundaries of austenite and ferrite phases. An average of 10 measurements per phase were taken. The uncertainty of the measured hardness was estimated to be ±15 HV.

2.3.2. Hardness model

The hardness increase caused by SD can be predicted by the Ardell screw dislocation hardening model [22] at 300 °C for SDSS 2507 [5]:

$$\Delta\tau_{CRSS} = N(A\eta Y)^{\frac{5}{3}}\left(\frac{\Lambda b}{\Gamma}\right)^{2/3} \quad (1)$$

where Γ (with a unit like Gb^2) is the line tension of a dislocation. The value of Γ and the numerical coefficient N are 0.591 and 0.041, respectively, for screw dislocations [22]. Then, the yield stress is converted to changes of ferrite hardness by [23]:

$$\Delta HV = \frac{M \times \Delta\tau_{CRSS}}{2.876} \quad (2)$$

where M is the Taylor factor for polycrystalline BCC metals and was found to be approximately equal to 2.733 [24]. In this work, using the values of amplitude (A) and wavelength (Λ) (quantified by SANS), the hardness changes can be predicted and then compared to the actual changes.

2.4. Small-angle neutron scattering (SANS)

2.4.1. Experimental details

SANS experiments were conducted at the LOQ beamline at the ISIS

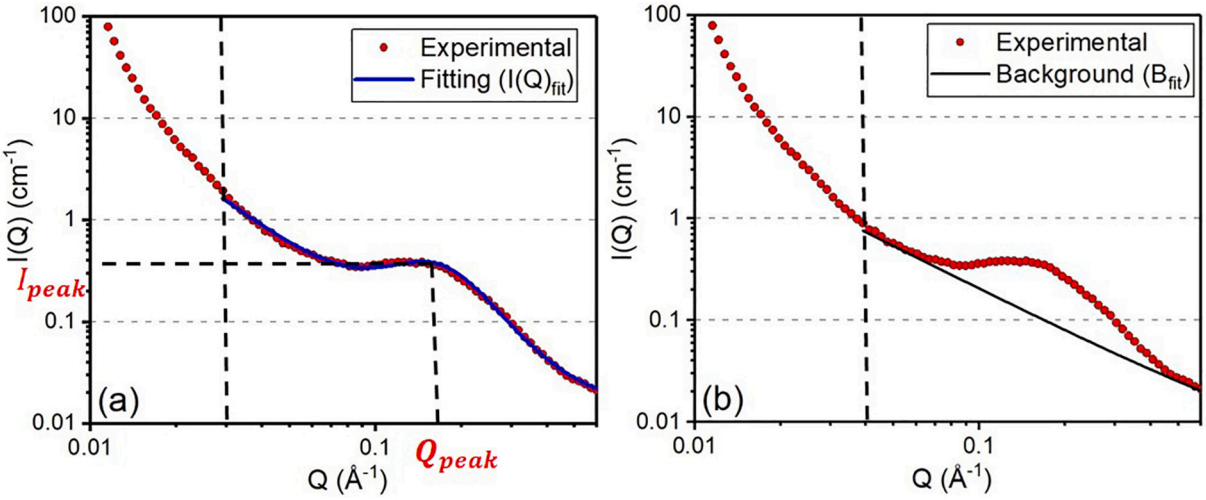

Fig. 1. Illustration of fitting (a) the complete scattering data and (b) the background.

Pulsed Neutron and Muon Source, UK. At the LOQ beamline the incident neutrons have wavelengths (λ) in the range of 2.2−10 Å, which enables scattering vectors ($Q = (4\pi \sin\theta)/\lambda$, where 2θ is the scattering angle) of 0.008−1.4 $Å^{-1}$ to be measured simultaneously [25]. The weldment samples for SANS experiments were cut from the upper part of the weld bead (which includes parts of the BM), with the dimensions 10 ×10 ×1.5 mm^3. Prior to the experiments, the samples were ground and polished to remove any surface oxide film that may have been present. The samples were positioned at about 11 m from the moderator and two detector banks were used to collect the scattered neutrons. The first is an annular scintillator area detector at 0.5 m from the sample with 12 mm resolution. The second detector is an ORDELA area detector (64 cm × 64 cm) filled with ^{3}He-CF_4 gas with a 5 mm resolution located 4.15 m from the sample area. The collimated neutron beam diameter was 6 mm and all measurements were conducted for ~2.5 h at ambient temperature.

2.4.2. Reduction and normalization of SANS data

MantidPlot framework (version 5.1.1) [26,27] was used to radially average the data from 2D to 1D after SANS data collection. The procedure corrected for efficiency and spatial linearity of the detectors, the neutron absorption of the sample (sample transmission), the instrumental background scattering and the illuminated gauge volume. The overall purpose of the above data reduction was to obtain the macroscopic coherent elastic differential scattering cross section ($d\Sigma(Q)/d\Omega$), colloquially referred to as the intensity I (unit: cm^{-1}) [25], as a function of Q. These data were then placed on an absolute scale by reference to the scattering from a calibration standard [28]. In order to extract the independent contribution of WM from the SANS signal, the fraction of WM in the neutron-illuminated area (6 mm-diameter neutron beam) was estimated from LOM images. This fraction of WM was subsequently used to normalize the scattering intensity to quantify PS in the WM. This data treatment enabled us to isolate the SANS signal from the WM, but the procedure is associated with an uncertainty estimated to be ~ 5%.

The method to quantifying the characteristic distance, i.e. wavelength (Λ), and compositional fluctuation, i.e. amplitude (A), has been described previously [20]. First, the reduced SANS data was normalized versus the background: using the SasView software (version 4.2.2) [29], a combination of a power-law background function [9,30] and a generalised spinodal function was fitted to describe the PS [31]:

$$I(Q)_{fit} = I(Q)_{spinodal} + B_{fit} \tag{3}$$

where $B_{fit} = A_{power\_law}Q^{-n} + B_g$, the prefactor A_{power_law} determines the relative contribution of that term, n is a power law exponent ($1.5 \leq n \leq 4$), and B_g is the residual Q-independent background level. The spinodal model used here is taken from the work of Furukawa [31] and is as follows:

$$I(Q)_{spinodal} = I_{peak}\left(1+\frac{\gamma}{2}\right)x^2 \Big/ \left(\frac{\gamma}{2}+x^{2+\gamma}\right) \tag{4}$$

where $x = Q/Q_{peak}$, Q_{peak} is the peak position and I_{peak} is the intensity at Q_{peak}, see Fig. 1 **(a)**. The term γ is equal to $d + 1$ or $2d$. Here, d is the dimensionality and 3 was used in this work. The fit of **Eq. (3)** to the SANS data is reasonably good [5,20,32], as shown in Fig. 1 **(a)** The normalized scattering intensity (NSI) was plotted in the following way to show the evolution: the $I(Q)_{fit}$ was first normalized by the background function B_{fit} (i.e., $\frac{I(Q)_{fit}}{B_{fit}}$) to reveal the shape of the underlying spinodal signal (I_n). This "I_n" was then fitted to a Gaussian function $S(Q)_{fit}$. The signal from PS was then obtained by removing the contribution of the background and normalizing it with respect to B_{fit} (see Fig. 1 **(b)**), i.e. $S(Q) = B_{fit}(S(Q)_{fit} - B_{fit}/B_{fit})$ [20],.

2.4.3. Quantification of SANS data

The method to quantify the SANS data has also been shown in our previous paper [20]. The wavelength (Λ) of the PS can be obtained from Q_{peak} using the simple expression: $\Lambda = 2\pi/Q_{peak}$. For the investigated samples, it is the ferrite in which the PS occurred and which contributes to the correlation peak in the SANS data. Thus, the volume fraction of the ferrite for the investigated samples was firstly analysed by EBSD. Then the amplitude quantification can be performed according to [20]:

$$I_{peak} = \varphi\,(1-\varphi)\left(\frac{\Lambda}{2}\right)^3(\Delta\rho)^2 \tag{5}$$

where φ is the volume fraction of the α' phase in the ferrite and $\Delta\rho$ is the neutron scattering length density (SLD) difference between the α and α' phases. The amplitude (A at. %) can be obtained by the following expression [20]:

$$A\ (at.\%) = \Delta\rho\frac{10\ at.\%}{0.5\times10^{-6}\text{Å}^{-2}} \tag{6}$$

The above method was recently successfully applied to a study of the amplitude and wavelength evolution in DSSs [5]. The main approximation involved is that the phase-separated domains are cubes with edge length $\Lambda/2$.

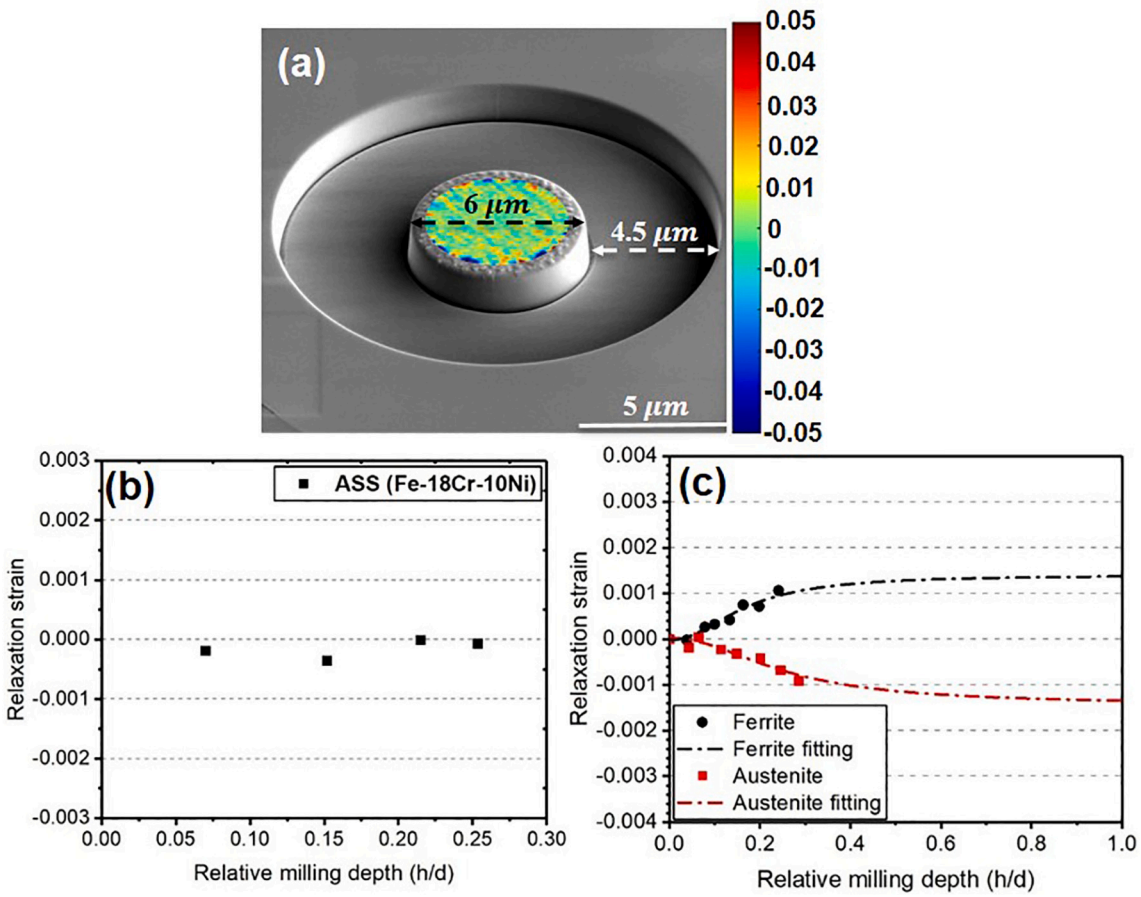

Fig. 2. (a) SEM image of a ring-core milled ferrite of DSS 2507; Normalized relaxation strain as a function of normalized relative depth for: (b) FIB ring-core drilling measurement of single-phase austenitic stainless steel; (c) FIB ring-core drilling measurement of DSS 2507 in the as-cooled state.

2.5. Focused ion beam – digital image correlation (FIB-DIC) for residual strain analysis

2.5.1. Experimental details

The FIB milling was performed in a FEI Nova 600 NanoLab. Prior to FIB-DIC analysis, specimens were finally electro-polished in 10% $HClO_4$ in a methanol solution using a voltage of 20 V for 2 min. Randomized surface patterns, consisting of irregular shapes with an overall external size of the patterned area of 7×7 μm^2,was generated on the sample surface at the region of interest through e-beam Pt deposition at 5 kV and 6.3 nA. Ion beam milling of annular rings was carried out at 30 kV and a low beam current of 0.3 nA in order to reduce beam damage and re-deposition at the core [33,34]. Secondary electron imaging after each milling step was captured with an image size of 2048×1887 pixels with 30 μs dwell time per pixel. The beam drift was monitored during milling and a correction was applied when necessary. An island diameter (d) of 6 μm and an annular trench width of 4.5 μm were selected to balance the milling time, accuracy of strain evaluation, and make it convenient to measure the height of the central pillar (real milling depth, h) [35], see Fig. 2 **(a)**. The image comparison between the pattern on the FIB ring drilled island with the undisturbed pattern were processed by Ncorr (version 1.2), which is an open source Matlab program for 2D digital image correlation (DIC) analysis [36]. This approach allowed the determination of the displacements of the deposited individual Pt shapes in the pattern, and hence the strain relief of the central pillar after each FIB milling to be computed. In this study, the FIB ring-core milling was performed on the ferrite of BM and weldments in the condition prior to low temperature aging. In total eight and five depths were milled step-wise on BM and weldments, respectively, to reach 0.3 in relative milling depth. The increment of each milling step was in the range of 200 to 300 nm.

2.5.2. Residual strain calculation and validation

Prior to the measurements on the DSS, the FIB-DIC methodology was validated by the following method: a hot-rolled single-phase austenitic stainless steel (ASS) Fe-18Cr-10Ni (wt%) was homogenized at 1100 °C for 10 min and slowly furnace cooled. This annealing was performed to minimize residual strains in the sample and reach a near strain-free state. The above-mentioned ring-core milling was performed on the sample and the distribution of strain on the surface of the central pillar after each milling step was calculated by Ncorr, see the demonstration in Fig. 2 **(a)**. Thereafter, those strain values were averaged out to obtain the total strain relief at each milling depth. In such case, the positive strain value (+) means the central pillar is stretched, and therefore the whole sample is compressed; On the contrary, the negative strain value (−) corresponds to the sample is stretched. The relaxation strain against relative milling depth ($D = h/d$) were plotted, see Fig. 2 **(b)**. The relaxation strain did not show obvious change with the increase of milling depth in the annealed sample. This shows that the FIB-DIC analysis is not prone to generate artificial strains in annealed single-phase samples and that the method could be suitable for the intended purpose in the present work. Due to the limitation of the austenite and ferrite phase size in this work, the maximum depth milled was only 1.5 μm in order to avoid the beam penetrating into the neighbouring phase and reduce the material re-deposition onto the core surface. In order to obtain the fully relaxed strain, the curve of milling depth versus strain was extrapolated by a non-linear curve fitting function:

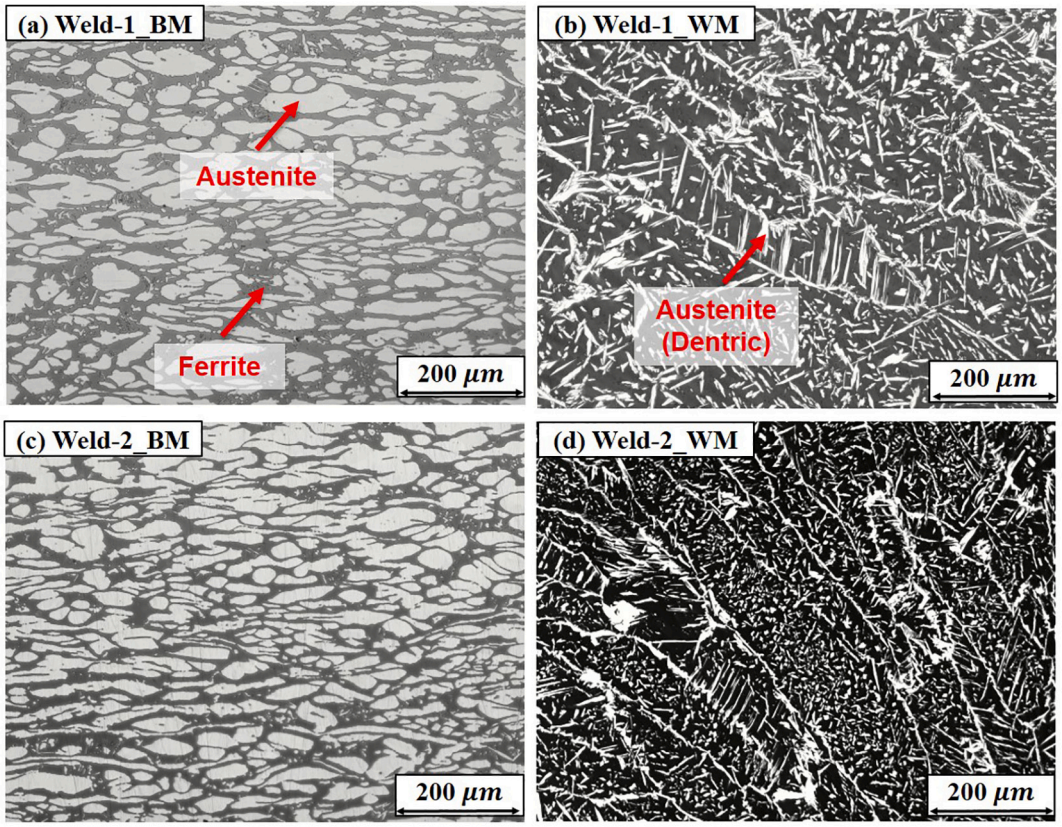

Fig. 3. LOM images of as-received Weld-1 (dark: ferrite; bright: austenite): (a) BM and (b) WM; and Weld-2: (c) BM and (d) WM.

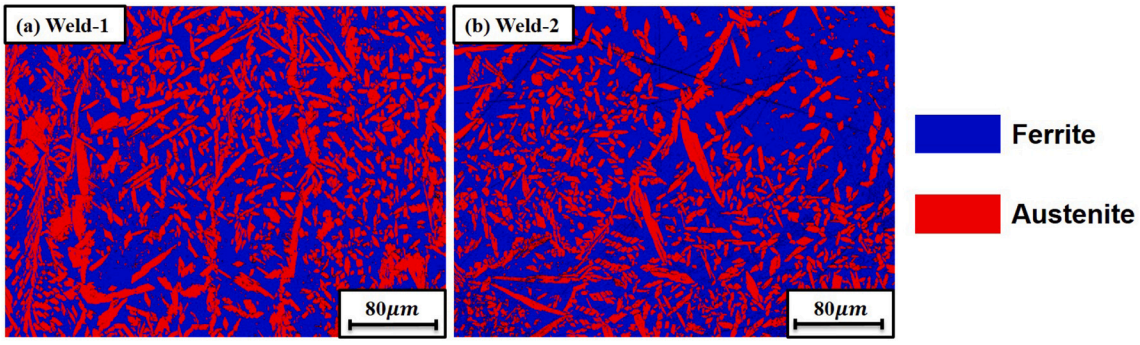

Fig. 4. EBSD phase maps of WM for (a) Weld-1 and (b) Weld-2 (blue and red colours represent ferrite and austenite, respectively). (For interpretation of the references to colour in this figure legend, the reader is referred to the web version of this article.)

Table 2
Volume fraction and grain size of different phases in the investigated materials.

Materials	Volume fraction (%)		Grain size (μm)	
	Ferrite	Austenite	Ferrite	Austenite
Weld-1	57.0 ± 0.4	43.0 ± 0.4	18.3 ± 0.2	12.9 ± 0.2
Weld-2	67.3 ± 0.5	32.7 ± 0.4	15.4 ± 0.2	11.6 ± 0.1
SDSS 2507 (BM) [32]	40.6	59.4	4.8	3.9

$$\Delta\varepsilon = \frac{A_1 - A_2}{1 + (D/D_0)^p} + A_2 \tag{8}$$

where A_1, A_2, D_0, p are fitting parameters. The fitting and extrapolation are shown in Fig. 2 **(c)**. Due to the difference of thermal expansion coefficient between austenite and ferrite [37], the initial residual strains are compressive (−) in the ferritic phase and tensile (+) in the austenitic phase. This is witnessed as positive relaxation strain values for ferrite and negative values for austenite. The goodness-of-fit was measured by the reduced chi-square (χ^2), for ferrite and austenite which are 1.16×10^{-8} and 1.80×10^{-8}, respectively. These fits and extrapolations are reasonably good, indicating a high correlation between the extrapolated strain and relative milling depth. From the extrapolation, the relaxation strains of ferrite and austenite are 1.35×10^{-3} and $-\ 1.37\times10^{-3}$, respectively. Both values are in reasonable agreement with previous studies [37,38].

3. Results

3.1. Microstructures

The LOM images of the two weldments are shown in Fig. 3, in which the ferrite is dark and the austenite appears bright. The BMs (Fig. 3 **(a)**

Table 3
Chemical composition of the two weldments and BM in the as-cooled state, quantified by EDS (wt%).

Samples	Area	Fe	Si	Mn	Cr	Ni	Mo	Cu
Weld-1	Bulk	60.1 ± 0.4	0.4 ± 0.1	0.5 ± 0.1	26.5 ± 0.2	7.9 ± 0.2	3.8 ± 0.1	0.8 ± 0.1
	FCC	59.7 ± 1.2	0.4 ± 0.1	0.5 ± 0.1	26.4 ± 0.3	8.5 ± 0.6	3.7 ± 0.1	0.9 ± 0.1
	BCC	60.3 ± 0.6	0.4 ± 0.1	0.5 ± 0.1	26.7 ± 1.0	7.5 ± 0.6	3.9 ± 0.4	0.8 ± 0.1
Weld-2	Bulk	61.0 ± 0.4	0.4 ± 0.2	0.5 ± 0.1	26.1 ± 0.2	7.5 ± 0.2	3.7 ± 0.6	0.9 ± 0.1
	FCC	60.7 ± 0.5	0.4 ± 0.1	0.5 ± 0.1	26.1 ± 0.6	8.0 ± 0.8	3.4 ± 0.4	0.9 ± 0.3
	BCC	61.5 ± 1.0	0.4 ± 0.1	0.4 ± 0.1	26.2 ± 0.6	7.1 ± 1.3	3.5 ± 0.6	0.8 ± 0.3
SDSS 2507 (BM)	Bulk	63.2 ± 0.2	0.3 ± 0.1	0.6 ± 0.1	25.0 ± 0.1	7.0 ± 0.1	3.0 ± 0.3	0.9 ± 0.1
	FCC	63.5 ± 0.4	0.3 ± 0.1	0.7 ± 0.1	24.0 ± 0.2	8.0 ± 0.3	2.6 ± 0.5	0.9 ± 0.1
	BCC	62.3 ± 1.2	0.4 ± 0.1	0.5 ± 0.1	25.9 ± 0.8	5.2 ± 0.4	4.0 ± 0.7	0.9 ± 0.3

and **(c)**) show elongated austenite grains in the rolling direction distributed in the ferrite matrix while the WMs (Fig. 3 **(b)** and **(d)**) have a typical solidification microstructure, containing a Widmanstätten-like austenite structure. The dendritic structure precipitated from ferrite grain boundary and align parallel to each other in the coarse ferrite matrix. Intragranular austenite was also observed in the WM. The ferrite fraction in WM increases compared to the BM for both weldments.

From the EBSD phase map of the welds (see Fig. 4), it can be seen that the welds have a matrix of coarse ferrite grains (blue) and dendritic austenite grains (red). In comparison, e.g. Xu et al. [32] presented the microstructure of hot-rolled SDSS 2507, where the austenite is lined up in rows as a banded structure. The volume fraction and the grain size of the ferrite and austenite in the two weldments are shown in Table 2, together with the results from the hot-rolled SDSS 2507 analysed in Xu et al. [32]. Weld-1 and Weld-2 have larger ferrite volume fraction than SDSS 2507 as well as larger grain size for austenite and ferrite. It is worth noting that the ferrite and austenite grain size (refer to Table 2) in Weld-1 is larger than in Weld-2, see Fig. 3 **(b)** and **(d)**, respectively.

The EDS results showing the chemical composition of the phases in the two weldments and BM in the as-cooled state are given in Table 3.

Table 4
Wavelength and amplitude of PS in the ferrite of SDSS 2507, Weld-1 and Weld-2.

Aging time (h)	Wavelength (nm)			Amplitude (at.%)		
	SDSS 2507	Weld-1	Weld-2	SDSS 2507	Weld-1	Weld-2
0	4.3±0.2	4.4 ±0.2	4.2 ±0.2	15.1 ±1.1	15.1 ±1.2	16.6 ±1.3
6000	4.1±0.2	3.9 ±0.2	4.2 ±0.2	16.9 ±1.2	19.6 ±1.4	21.8 ±1.5
12,000	4.0±0.2	3.9 ±0.2	4.1 ±0.2	17.7 ±1.3	30.1 ±1.7	32.5 ±1.6
24,000	3.9±0.1	–	–	19.8 ±1.3	–	–
35,000	–	4.0 ±0.1	4.2 ±0.1	–	43.9 ±1.8	48.1 ±1.9
48,000	3.9±0.1	–	–	26.0 ±1.5	–	–

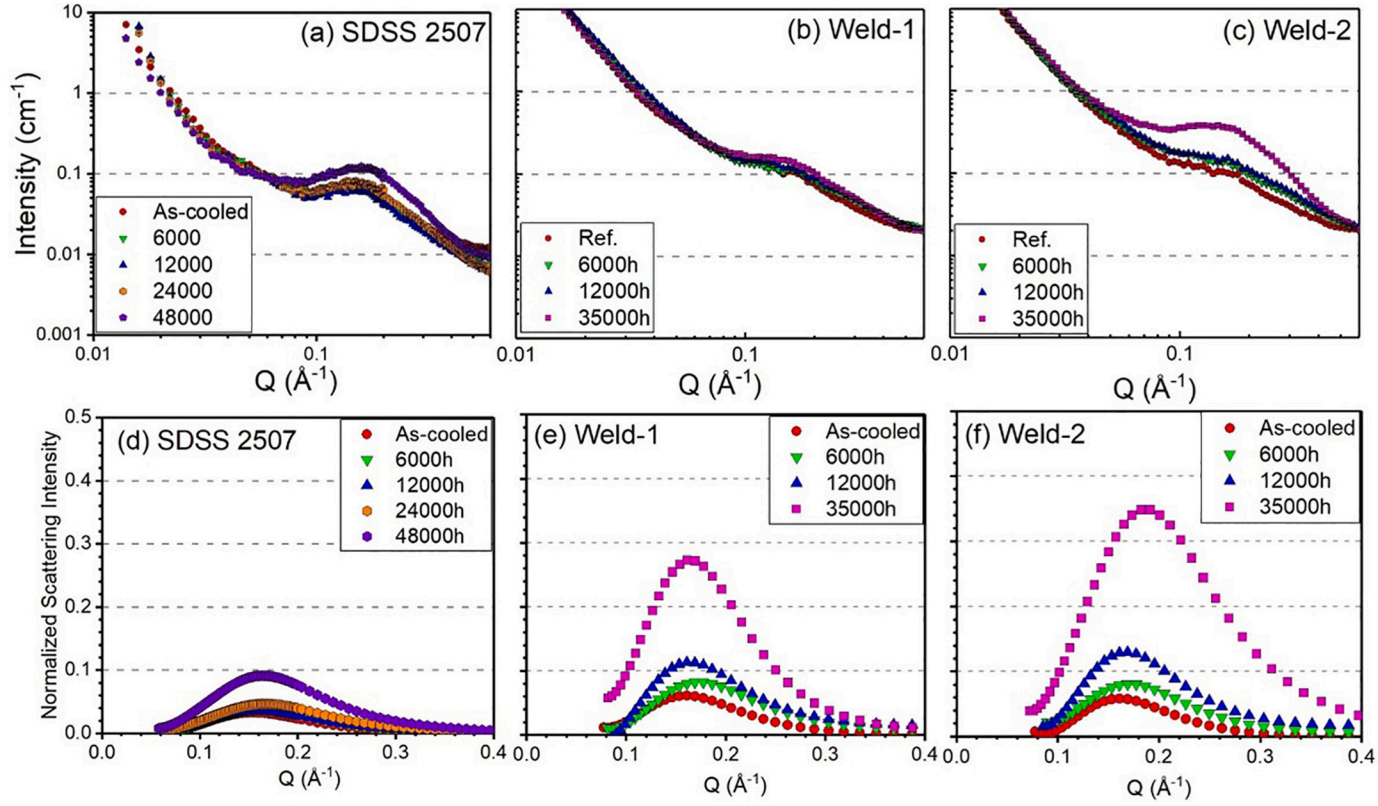

Fig. 5. The 1D reduced SANS data during aging at 300 °C from (a) SDSS 2507 (adapted figure from Ref. [5]); (b) Weld-1 and (c) Weld-2; NSI from (d) SDSS 2507 (adapted figure from Ref. [5]), (e) Weld-1 and (f) Weld-2,

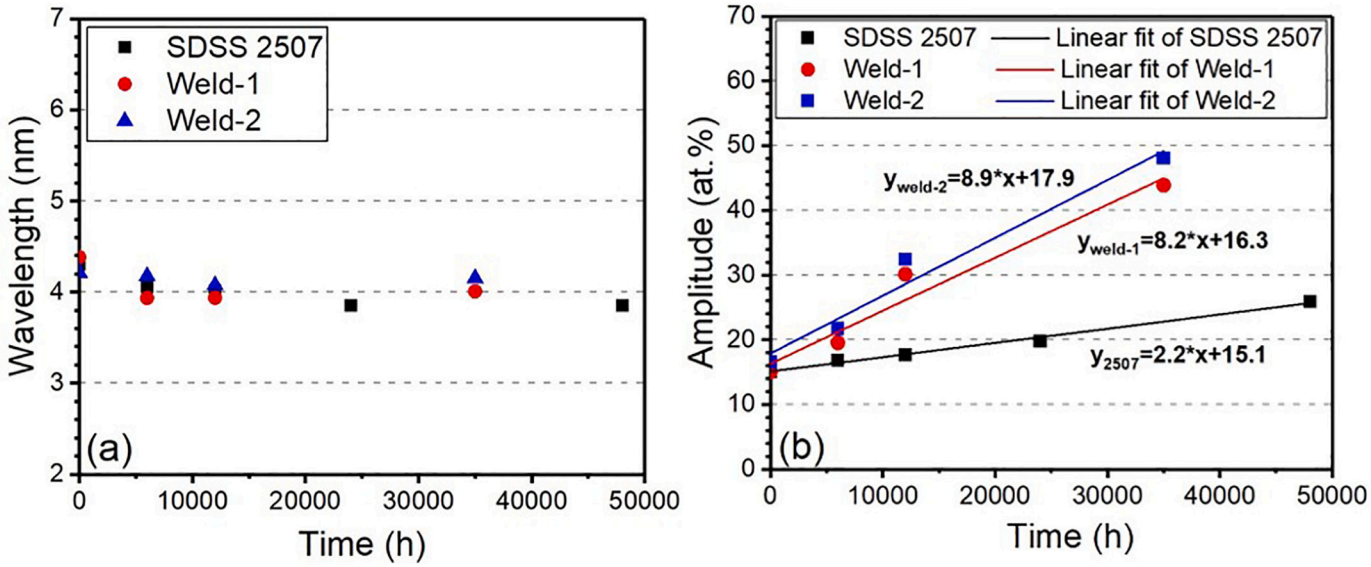

Fig. 6. (a) Wavelength and (b) amplitude (with linear fitting) of PS in the ferrite of SDSS 2507, Weld-1 and Weld-2.

For the bulk composition, the contents of Cr and Ni are quite close to the as-received nominal composition (Table 1) for all three kinds of samples, whilst the Cu and Si contents are slightly higher and the Mo and Mn are slightly lower. In the ferrite phase of each specimen, Weld-1 and Weld-2 clearly have higher Ni content than the SDSS 2507, as well as slightly higher Cr contents. The Ni content in the austenite phases is higher than that in the ferrite for all the investigated samples, especially in the case of Weld-1 (8.45 wt%). Conversely, the Cr content of the austenite phase is slightly lower in all samples.

3.2. SANS quantification

The SANS data for the investigated samples are shown in Fig. 5. In general, the correlation peaks of all investigated samples evolve with an increase of aging time for all specimens, see Fig. 5 **(a)-(c)**. For SDSS 2507 (Fig. 5 **(d)**), it is hard to distinguish the difference in the NSI from 0 to 24,000 h and the NSI peak is clearly higher only after 48,000 h aging. For the two weldments (Fig. 5 **(e) (f)**), the NSIs overlap until 6000 h and then the peaks evolve more significantly. The NSI of Weld-1 at 12000 h is close to that of SDSS 2507 at 48000 h, indicating a similar degree of PS. Moreover, at the aging time of 12,000 h, Weld-2 shows higher peaks than Weld-1. For the prolonged aging time, Weld-1 and Weld-2 both show an obvious increase of NSI at 35000 h aging, in which the NSI peak of Weld-2 is higher than that of Weld-1. The NSIs of the two weldments are much higher than that of the SDSS 2507, even though 2507 experienced a longer aging time (48,000 h). Hence, the two weldments show significantly faster kinetics of PS as compared to the BM. The accelerating effect becomes apparent at least after 12,000 h aging and, significantly more severe PS is observed after 35,000 h.

The values of wavelength and amplitude are presented in Table 4 and plotted in Fig. 6. A decrease of wavelength is observed during aging up to 12,000 h for each sample, decreasing by 0.3 nm (7.0%) for 2507, 0.5 nm (11.4%) for Weld-1, 0.1 nm (2.4%) for Weld-2, respectively. Then after aging for 35,000 h, slight increases (0.1 nm) of wavelength for both Weld-1 and Weld-2 are observed (2.6% for Weld-1 and 2.4% for Weld-2, respectively), meanwhile the wavelength of SDSS 2507 remains the same until 48,000 h. As shown in Fig. 6 **(a)**, in general, the fluctuations of wavelength are minor, as the PS is still in the early stage. Regarding the change in amplitude, the increase for SDSS 2507 is only 10.9 at.% over the whole aging period, while, for the two weldments, a rapid increase of amplitude was observed after only 12,000 h aging, both values of which are even higher than the amplitude of SDSS 2507 aged for 48,000 h (26.0 at.%). Finally, after 35,000 h aging, the amplitude of Weld-1 and Weld-2 increased to 48.3 at.% and 56.6 at.%, respectively. The amplitude evolution in the two weldments is much more significant than in the BM, increasing by 33.2 at.% and 40.0 at.%, respectively. Correspondingly, in Fig. 6 **(b)**, it is shown that the slopes of linear fits for SDSS 2507, Weld-1 and Weld-2 are 2.2, 8.2 and 8.9, respectively, indicating faster kinetics of PS in the two weldments compared to SDSS 2507. The trends of the amplitude evolution correlate well with the NSI evolution shown in Fig. 5.

3.3. Micro-hardness

The micro-hardness of ferrite and austenite are shown in Fig. 7. The micro-hardness of the austenitic phase remained close to constant during aging for the two weldments, see Fig. 7 **(a)**. It is worth noting that the two weldments show slightly higher micro-hardness of austenite than BM, which is most likely due to the higher content of Cr and Ni elements from the filler material introduced during the welding. On the other hand, there were observable increases in the ferrite hardness with increasing aging time for both BM and the two weldments, see Fig. 7 **(b).** When the aging time is lower than 12,000 h, ferrite in all samples experienced significant hardening, and the two weldments had higher hardness as well as hardening rate than the BM. The increase of ferrite micro-hardness of the the BM was 40.7% after aging for 12,000 h, while the values were 50.7% for Weld-1 and 51.0% for Weld-2. It is observed that in the as-cooled state, the initial ferrite hardness for BM and the two weldments are similar. However, the ferrite hardness of the two weldments increases faster, and the rate of hardening accelerates with the increase of aging time (within 12,000 h). Then, the hardening rate of all three samples reduced after 12,000 h: the increase of ferrite hardness were 13.6% for Weld-1 and 14.3% for Weld-2. Nevertheless, they are still larger than that of BM (10.5%), even though the aging time of BM was longer (48,000 h). Fig. 7 **(c)** shows the predicted hardness increase of ferrite in two weldments by Ardell-screw model [22] and the comparison to the actual experimental hardness change (The predicted ferrite hardness increase of SDSS 2507 at 300 °C can be seen in **Fig. 10** from Ref. [5]). It was observed that the predicted hardness increase are in good agreement with the experimental results, even though this model has slightly underestimated the hardness increase.

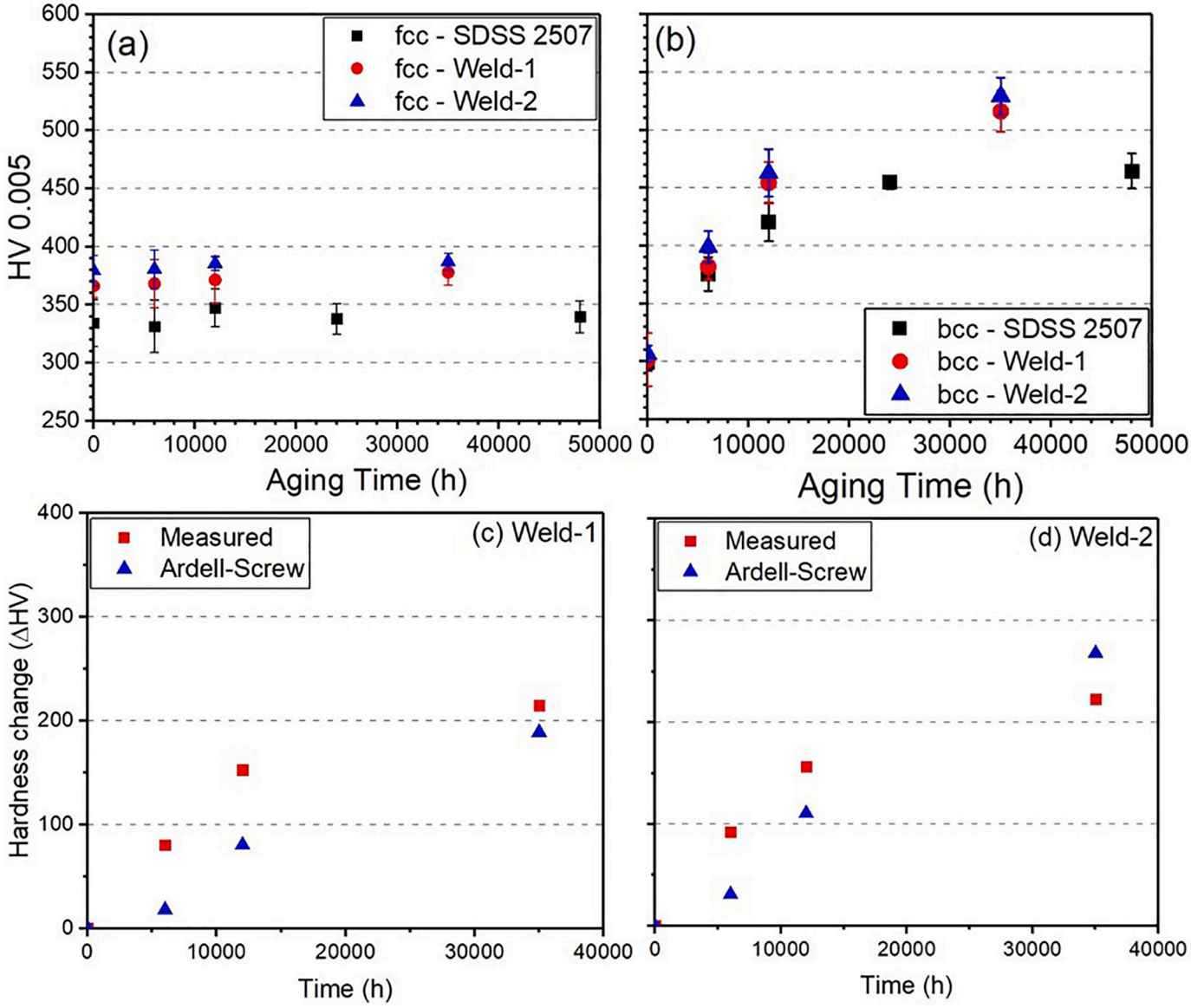

Fig. 7. Micro-hardness of SDSS 2507, Weld-1 and Weld-2 for (a) austenite and (b) ferrite, respectively; Comparison between the measured changes in hardness (from Fig. 7 (b)) and model predictions based on the Ardell [22] approaches (input parameters, i.e. wavelength and amplitude, are from Table 4) following aging of (c) Weld-1 and (d) Weld-2 at 300 °C.

3.4. Residual strain

The relaxation strain profiles of the ferrite are shown in Fig. 8, in which the fully relaxed strains for Weld-1 and Weld-2 are estimated as 3.05×10^{-3} and 4.7×10^{-3}, respectively. The values of χ^2 for SDSS 2507, Weld-1 and Weld-2 are 1.16×10^{-8}, 1.31×10^{-8} and 1.51×10^{-8}, respectively, which are low enough to show a high correlation between extrapolated strain and relative milling depth. Therefore, it can be clearly seen that the sequence of relaxation strain in ferrite (from large to small in absolute value) is Weld-2 > Weld-1 > SDSS 2507.

4. Discussion

4.1. Phase separation and hardness response

The long-term isothermal aging of base metal SDSS 2507 and weldments Weld-1 and Weld-2 at 300 °C lead to an evolution in Cr fluctuation within the ferrite phase. The weldments show slightly higher NSI than the BM for the non-aged samples (see Fig. 5). Since the slight Cr fluctuation was previously observed for the unaged SDSS 2507 [5,39], it indicates that the welding process would lead to more Cr clustering and possibly PS, since it is most likely kept longer time within the miscibility gap. During the subsequent aging, the more pronounced nanostructural evolution in the weldments than in the BM shows that the TIG welding accelerated the kinetics of PS in SDSS especially for prolonged holding at low temperature. This is in agreement with the APT study by Zhou et al. [12]. The carbon content is very low (see Table 1) so carbide formation should therefore not contribute significantly to hardening. Moreover, no other precipitates e.g. intermetallics have been observed, see Fig. 3. Hence, the increase of ferrite micro-hardness is primarily due to the evolution in Cr amplitude, which can be predicted by a suitable hardening model [5]. Here the sequence of hardening rate from high to low is Weld-2 > Weld-1> SDSS 2507, which is in good agreement with the increase of Cr amplitude (refer to Table 4). It is concluded that the TIG welding accelerated the kinetics of PS and therefore, accelerated the hardening rate of SDSS 2507.

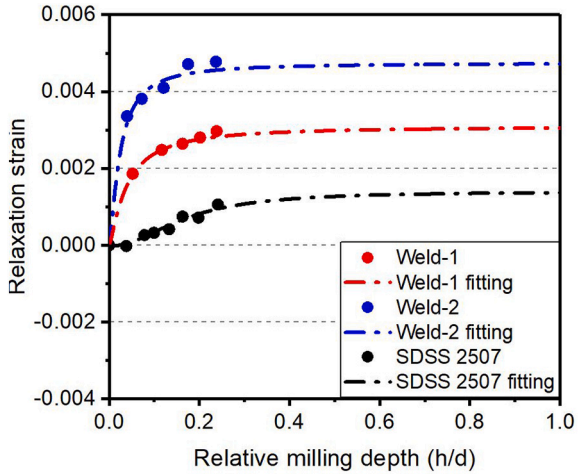

Fig. 8. FIB ring-core drilling measurements on the ferrite of SDSS 2507 and weldments Weld-1 and Weld-2 in as-cooled state (normalized strain relief as a function of normalized milling depth).

4.2. Alloying element effect on phase separation

The faster rate of PS in weldments could be due to their higher Cr and Ni content compared to the SDSS 2507. The accelerating effect of alloying elements, e.g. Cr [32] and Ni [7,40,41], on the rate of PS in Fe—Cr based alloys has been reported before, although in this work the difference of Cr content is minor. The contents of Mo, Si, Cu and Mn only show minor differences between the weldments and BM, so their effects on the kinetics of PS should be negligible. However, when only comparing the weldments, Weld-2 shows faster kinetics of PS, as well as hardening rate, than Weld-1 at the same aging time, which clearly becomes more pronounced with increasing aging time. These two weldments were both welded from the SDSS 2507 by the TIG welding technique using the same filler material, and the chemical composition analysis of the weldments showed that the contents of Cr, Ni and Mo are even slightly higher in the ferrite of Weld-1 (see Table 3). Hosseini et al. [11] have claimed that for PS, the influence of processing route is more crucial than slight variations in composition. Here it should be kept in mind that Weld-2 has had a higher heat input in each welding pass so the effect of different welding protocols is discussed next.

4.3. Residual strain effect on phase separation

The more severe PS of the weldments could also be due to the introduced residual strains during the welding process itself, with expected high internal strains promoting PS. It was reported that austenite would experience more expansion than ferrite when heated to the welding temperature range [37] and therefore the ferrite will experience compressive strains after cooling. Hosseini et al. [11] observed a higher density of dislocations next to the austenite phase boundary which promotes the PS, which correlates to the higher residual strains in the ferrite in this work and therefore leads to the increase of PS kinetics. Dahlström et al. [42] studied the pure elastic stress effect on PS by APT and phase-field modeling, and found that spinodal decomposition is more severe with higher applied external tensile stress in Fe-35 at.%Cr system. In addition, the accelerated kinetics of PS in Weld-2 than Weld-1 is most probably due to the different welding protocols. Weld-2 experienced fewer welding passes, but each pass had a higher average heat input although the total heat input was almost the same. The higher heat input in each pass would lead to more residual strains, resulting in higher internal strains (see Fig. 8) and therefore promoting PS [12]. Moreover, the more welding passes in Weld-1 (15 passes) will lead to a more pronounced tempering effect to the prior passes during TIG welding [43], which could relieve the strains imposed from welding to some extent and thus lower the rate of PS.

5. Conclusions

This paper has compared the kinetics of phase separation on base metal SDSS 2507 and TIG-welded SDSS weldments subjected to isothermal long-term aging at 300 °C. Phase separation occurs within ferrite in the investigated alloys under the experimental conditions. The increase in hardness is caused by the nanostructural Cr fluctuations within the ferrite phase. Moreover, EDS and FIB-DIC analysis were performed to further investigate the underlying mechanism of the accelerated rate of PS. Key findings are summarised below:

1) The TIG welding can promote subsequent phase separation and hardening in super DSS at the application temperature, especially during prolonged aging;
2) The cause of pronounced phase separation in weldments is partly attributed to the higher internal residual strains in the weldments imposed by the welding process; and, the higher content of Cr and Ni in the weldment compared to the base metal also contribute to higher rate of phase separation;
3) The heat input per pass during TIG welding is shown to have an effect on the kinetics of phase separation with a more pronounced phase separation for the weld with higher heat input.

Data availability

The data that support the findings of this study are available from the corresponding author upon reasonable request.

Declaration of Competing Interest

The authors declare that they have no known competing financial interests or personal relationships that could have appeared to influence the work reported in this paper.

Acknowledgement

The project Cooler was financed by Vinnova under contract 2015–03453 within the Strategic Swedish Innovation Programme for Metallic Materials 2013–2016 and the Swedish industry. The EIT Raw-Materials EndureIT project is acknowledged for financial support. The authors also acknowledge the award of beamtime (Experiment No. 1810590, DOI: https://doi.org/10.5286/ISIS.E.RB1810590) at the STFC ISIS Pulsed Neutron & Muon Source, UK. J. Liu acknowledges Dr. Benjamin Neding at KTH for providing the austenitic stainless steel and Stella Sten at KTH for assisting EDS measurements. Dr. Wangzhong Mu at KTH is acknowledged for valuable discussion. J. Liu thanks the China Scholarship Council (CSC No.201700260207) and Jernkontoret Forskningsstipendium for financial support. Y. Das acknowledges Olle Eriksson travel grant. This work benefited from the use of the SasView application, originally developed under NSF award DMR-0520547. SasView also contains code developed with funding from the European Union's Horizon 2020 research and innovation programme under the SINE2020 project, grant agreement No 654000.

References

[1] J.-O. Nilsson, Super duplex stainless steels, Mater. Sci. Technol. 8 (8) (1992) 685–700.
[2] J.K. Sahu, U. Krupp, R.N. Ghosh, H.J. Christ, Effect of 475°C embrittlement on the mechanical properties of duplex stainless steel, Mater. Sci. Eng. A 508 (1–2) (2009) 1–14.
[3] J. Tucker, M. Miller, G. Young, Assessment of thermal embrittlement in duplex stainless steels 2003 and 2205 for nuclear power applications, Acta Mater. 87 (2015) 15–24.

[4] C. Pareige, S. Novy, S. Saillet, P. Pareige, Study of phase transformation and mechanical properties evolution of duplex stainless steels after long term thermal ageing (> 20 years), J. Nucl. Mater. 411 (1–3) (2011) 90–96.
[5] Y. Das, J. Liu, H. Ehteshami, J. Odqvist, N. Holländer Pettersson, S. Wessman, S. King, P. Hedström, Quantitative nanostructure and hardness evolution in duplex stainless steels: under real low-temperature service conditions, Metall. Mater. Trans. A (2021) 1–13.
[6] M. Guttmann, Intermediate temperature aging of duplex stainless steels. A review, in: Duplex Stainless Steels'91 vol. 1, 1991, pp. 79–92.
[7] P. Hedström, F. Huyan, J. Zhou, S. Wessman, M. Thuvander, J. Odqvist, The 475°C embrittlement in Fe–20Cr and Fe–20Cr–X (X=Ni, cu, Mn) alloys studied by mechanical testing and atom probe tomography, Mater. Sci. Eng. A 574 (2013) 123–129.
[8] X. Xu, J. Odqvist, M.H. Colliander, S. King, M. Thuvander, A. Steuwer, P. Hedström, Effect of cooling rate after solution treatment on subsequent phase separation during aging of Fe-Cr alloys: a small-angle neutron scattering study, Acta Mater. 134 (2017) 221–229.
[9] X. Xu, J.E. Westraadt, J. Odqvist, T.G. Youngs, S.M. King, P. Hedström, Effect of heat treatment above the miscibility gap on nanostructure formation due to spinodal decomposition in Fe-52.85 at.% Cr, Acta Mater. 145 (2018) 347–358.
[10] H. Ramanarayan, T. Abinandanan, Phase field study of grain boundary effects on spinodal decomposition, Acta Mater. 51 (16) (2003) 4761–4772.
[11] V.A. Hosseini, M. Thuvander, K. Lindgren, J. Oliver, N. Folkeson, D. Gonzalez, L. Karlsson, Fe and Cr phase separation in super and hyper duplex stainless steel plates and welds after very short aging times, Mater. Des. 210 (2021), 110055.
[12] J. Zhou, J. Odqvist, M. Thuvander, S. Hertzman, P. Hedström, Concurrent phase separation and clustering in the ferrite phase during low temperature stress aging of duplex stainless steel weldments, Acta Mater. 60 (16) (2012) 5818–5827.
[13] L. Karlsson, Welding duplex stainless steels-a review of current recommendations, Weld. World 56 (5) (2012) 65–76.
[14] A. Vinoth Jebaraj, L. Ajaykumar, C.R. Deepak, K.V.V. Aditya, Weldability, machinability and surfacing of commercial duplex stainless steel AISI2205 for marine applications – a recent review, J. Adv. Res. 8 (3) (2017) 183–199.
[15] J. Verma, R.V. Taiwade, Effect of welding processes and conditions on the microstructure, mechanical properties and corrosion resistance of duplex stainless steel weldments—a review, J. Manuf. Process. 25 (2017) 134–152.
[16] S. Hertzman, R. Blom, Internal Report of the Swedish Institute of Metal Research (now Swerim AB), 2003, p. 542.
[17] V.A. Hosseini, M. Thuvander, S. Wessman, L. Karlsson, Spinodal decomposition in functionally graded super duplex stainless steel and weld metal, Metall. Mater. Trans. A 49 (7) (2018) 2803–2816.
[18] V. Hosseini, K. Hurtig, L. Karlsson, Effect of multipass TIG welding on the corrosion resistance and microstructure of a super duplex stainless steel, Mater. Corros. 68 (4) (2017) 405–415.
[19] V.A. Hosseini, S. Wessman, K. Hurtig, L. Karlsson, Nitrogen loss and effects on microstructure in multipass TIG welding of a super duplex stainless steel, Mater. Des. 98 (2016) 88–97.
[20] Y. Das, J. Liu, S. Wessman, X. Xu, J. Odqvist, S. King, P. Hedström, Small-angle neutron scattering quantification of phase separation and the corresponding embrittlement of a super duplex stainless steel after long-term aging at 300° C, Materialia 12 (2020), 100771.
[21] J.E. Westraadt, E.J. Olivier, J.H. Neethling, P. Hedström, J. Odqvist, X. Xu, A. Steuwer, A high-resolution analytical scanning transmission electron microscopy study of the early stages of spinodal decomposition in binary Fe–Cr, Mater. Charact. 109 (2015) 216–221.
[22] A.J. Ardell, Precipitation hardening, Metall. Trans. A. 16 (12) (1985) 2131–2165.
[23] E. Pavlina, C. Van Tyne, Correlation of yield strength and tensile strength with hardness for steels, J. Mater. Eng. Perform. 17 (6) (2008) 888–893.
[24] J. Rosenberg, H. Piehler, Calculation of the Taylor factor and lattice rotations for bcc metals deforming by pencil glide, Metall. Trans. A. 2 (1) (1971) 257–259.
[25] R. Heenan, J. Penfold, S. King, SANS at pulsed neutron sources: present and future prospects, J. Appl. Crystallogr. 30 (6) (1997) 1140–1147.
[26] O. Arnold, J.-C. Bilheux, J. Borreguero, A. Buts, S.I. Campbell, L. Chapon, M. Doucet, N. Draper, R.F. Leal, M. Gigg, Mantid—data analysis and visualization package for neutron scattering and μ SR experiments, Nucl. Instrum. Methods Phys. Res. Sect. A 764 (2014) 156–166.
[27] Manipulation and Analysis Toolkit for Instrument Data, Mantid Project, 2013, https://doi.org/10.5286/SOFTWARE/MANTID.
[28] G.T. Wignall, F.S. Bates, Absolute calibration of small-angle neutron scattering data, J. Appl. Crystallogr. 20 (1) (1987) 28–40.
[29] http://www.sasview.org.
[30] B. Hammouda, Probing Nanoscale Structures-the SANS Toolbox, National Institute of Standards and Technology, Center for Neutron Research, Gaithersburg, MD, USA, 2016.
[31] H. Furukawa, Dynamics-scaling theory for phase-separating unmixing mixtures: growth rates of droplets and scaling properties of autocorrelation functions, Physica A 123 (2–3) (1984) 497–515.
[32] X. Xu, S. Wessman, J. Odqvist, S.M. King, P. Hedström, Nanostructure, microstructure and mechanical properties of duplex stainless steels 25Cr-7 Ni and 22Cr-5Ni (wt.%) aged at 325° C, Mater. Sci. Eng. A 754 (2019) 512–520.
[33] A.M. Korsunsky, M. Sebastiani, E. Bemporad, Focused ion beam ring drilling for residual stress evaluation, Mater. Lett. 63 (22) (2009) 1961–1963.
[34] A.M. Korsunsky, M. Sebastiani, E. Bemporad, Residual stress evaluation at the micrometer scale: analysis of thin coatings by FIB milling and digital image correlation, Surf. Coat. Technol. 205 (7) (2010) 2393–2403.
[35] A.J. Lunt, N. Baimpas, E. Salvati, I.P. Dolbnya, T. Sui, S. Ying, H. Zhang, A. K. Kleppe, J. Dluhoš, A.M. Korsunsky, A state-of-the-art review of micron-scale spatially resolved residual stress analysis by FIB-DIC ring-core milling and other techniques, J. Strain Anal. Eng. Des. 50 (7) (2015) 426–444.
[36] http://www.ncorr.com/index.php.
[37] J. Johansson, M. Odén, X.H. Zeng, Evolution of the residual stress state in a duplex stainless steel during loading, Acta Mater. 47 (9) (1999) 2669–2684.
[38] P. Tao, J.-M. Gong, Y.-F. Wang, Y. Jiang, Y. Li, W.-W. Cen, Characterization on stress-strain behavior of ferrite and austenite in a 2205 duplex stainless steel based on nanoindentation and finite element method, Results Phys. 11 (2018) 377–384.
[39] N. Pettersson, S. Wessman, M. Thuvander, P. Hedström, J. Odqvist, R.F. A. Pettersson, S. Hertzman, Nanostructure evolution and mechanical property changes during aging of a super duplex stainless steel at 300°C, Mater. Sci. Eng. A 647 (2015) 241–248.
[40] B. Trindade, R. Vilar, Influence of nickel on 475° C embrittlement of Fe– Cr– Ni alloys: Mössbauer effect study, Hyperfine Interact. 66 (1–4) (1991) 351–358.
[41] M. Miller, K. Russell, Comparison of the rate of decomposition in Fe-45% Cr, Fe-45% Cr-5% Ni and duplex stainless steels, Appl. Surf. Sci. 94 (1996) 398–402.
[42] A. Dahlström, F. Danoix, P. Hedström, J. Odqvist, H. Zapolsky, Effect of stress on Spinodal decomposition in binary alloys: atomistic modeling and atom probe tomography, Metall. Mater. Trans. A 53 (1) (2022) 39–49.
[43] Y. Wan, W. Jiang, M. Song, Y. Huang, J. Li, G. Sun, Y. Shi, X. Zhai, X. Zhao, L. Ren, Distribution and formation mechanism of residual stress in duplex stainless steel weld joint by neutron diffraction and electron backscatter diffraction, Mater. Des. 181 (2019), 108086.